Supplementary material

Emission control redirects aerosol formation toward nocturnal oxidant chemistry: Observations at a Korean petrochemical complex

Jaeuk Kim[1], Sungjin Park[1], Jihye Moon[1], Jaewon Seo[1], Jungho Yu[2], Seonjin Yoon[2], Jeungwoon Kim[2], and Hwajin Kim[1]

[1]Department of Environmental Health Science, Graduate School of Public Health, Seoul National University, Seoul, South Korea
[2]Institute of Health and Environmental Research, Chungcheongnam-do, 8 Hongyegongwon-ro, Hongvuk-eup, Hongseoung-gun, Chungcheongnam-do, 32254, Republic of Korea

Correspondence to: Hwajin Kim (khj0116@snu.ac.kr)

SI 1 OA characteristics and source apportionment

Atmospheric OA are composed of complex materials that originate from different sources and have undergone different atmospheric processes. Understanding the chemical composition and sources of OA is important for understanding the impacts of these aerosols.

Separation of distinct organic aerosol sources can be achieved through the application of multivariate models such as PMF. In this study, four OA factors were determined, consisting of two POA factors (HOA and SFOA) and two SOA factors (LO-OOA and MO-OOA). The O/C ratios for the factors were MO-OOA=1.04, LO-OOA=0.53, SFOA=0.24 and HOA=0.11. The elemental ratios of the factors were estimated using the updated method reported by (Canagaratna et al., 2015). An overview of the chemical composition of and temporal variations in the four factors is shown in Fig. 2.

The four factors made similar contributions to total OA mass, with MO-OOA (36%) representing the largest fraction of the OA mass and the smallest fraction accounted for by LO-OOA, SFOA and HOA accounted for 27, 21 and 16% of total OA mass, respectively. Together, primary components on average accounted for 37% of the total OA mass and SOA accounted for 63% (Fig. S3a). The chemical composition of and temporal variations in each factor are discussed in detail below.

Hydrocarbon-like OA (HOA)

Alkyl fragments (CnH2n+1+ and CnH2n-1+) made a substantial contribution to the HOA factor, with major peaks at m/z 41, 43, 55 and 57, which were mostly composed of $C_3H_5^+$, $C_3H_7^+$, C_4H_{7+} and $C_4H_9^+$ ions, respectively (Fig. 2a). These major peaks and the overall picket-fence fragmentation pattern resulting from the CnH2n+1+ ions are typical features of the HOA spectra reported in other studies and are due to the association of these aerosols with fossil fuel combustion (Alfarra et al., 2007; Huang et al., 2010; Lanz et al., 2008; Morgan et al., 2010; Ng et al., 2011; Sun et al., 2011; Zhang et al., 2005). In addition, strong correlations were observed between the time series of HOA and the $C_nH_{2n+1}^+$ and $C_nH_{2n-1}^+$ ions, e.g., $C_4H_9^+$ (r=0.96), $C_5H_{11}^+$ (r=0.95), $C_6H_{11}^+$ (r=0.93) and $C_3H_7^+$ (r=0.92) (Fig. 2i). Due to

the dominance of chemically reduced hydrocarbon species, the O/C ratio of the HOA in this study was low (0.11), whereas the H/C ratio was high (2.01). The O/C ratio of HOA in this study was similar to the updated values of HOA (0.05-0.25) from other studies (Canagaratna et al., 2015).

The regular enhancement of HOA between 07:00 and 09:00, as shown in its diurnal profile (Fig. 2e), was consistent with the morning rush-hour traffic in Daesan, suggesting a contribution from vehicular emissions. HOA concentrations decreased rapidly from 09:00 to 13:00 and remained low in the afternoon, primarily due to atmospheric dilution associated with the rising mixing layer height (MLH). A gradual increase in HOA began around 19:00, likely reflecting the combined effects of evening traffic and a lowering MLH. The sustained emissions from industrial activities, together with meteorological influences, appeared to shape this pattern, while the concentration decrease observed between 23:00 and 03:00 likely reflects both a reduction in local primary emissions (e.g., vehicle activity) and enhanced atmospheric dispersion.

However, the time series correlations between HOA and other primary combustion tracers were only moderate, with BC showing a correlation coefficient of r = 0.38 and NO_2 showing r = 0.53 (Fig. S9a-b). This may be due to the fact that these species originate from multiple combustion-related sources in the region, including not only vehicles but also petrochemical operations and biomass burning. In contrast, stronger correlations were observed between these tracers and total POA (i.e., HOA + SFOA) (r = 0.52-0.56; Fig. S9c-d), reflecting the broader source contributions to POA.

Among the VOCs measured at the same site, toluene (C_7H_8) showed a correlation with HOA (r = 0.58), suggesting a common source (Fig. S10a). Given that toluene is a well-known marker for petrochemical process and vehicle emissions, this finding indicates that HOA in the Daesan area may be significantly influenced by emissions from nearby petrochemical facilities, in addition to traffic-related sources.

In the polar plot, HOA exhibited dominant influences from the east and southeast, consistent with the pattern observed for LO-OOA (Fig. S6). These directions correspond to areas adjacent to the sampling site where petroleum refining, petrochemical production, incineration facilities, and carbon black manufacturing processes are located. In addition, major roads with heavy traffic associated with industrial transportation pass through these areas. This spatial correspondence supports the interpretation that HOA originates from anthropogenic combustion sources linked to industrial and vehicular activities.

Solid Fuel OA (SFOA)

The SFOA (Solid Fuel Organic Aerosol) factor identified at the sampling site exhibited distinct characteristics indicative of solid fuel combustion. Its mass spectra were dominated by alkyl fragments ($C_nH_{2n+1}^+$ and $C_nH_{2n-1}^+$), commonly associated with fossil fuel combustion, and included significant biomass burning tracers such as m/z 60 ($C_2H_4O_2^+$) and m/z 73 ($C_3H_5O_2^+$). The factor also showed prominent signals of polycyclic aromatic hydrocarbons (PAHs), with a strong correlation between the SFOA time series and PAH-related fragments m/z 105 and 115 (r = 0.86), suggesting substantial contributions from incomplete combustion processes (Allan et al., 2010; Jeon et al., 2023; Tobler et al., 2021). The H/C and O/C ratios of SFOA were 1.82 and 0.24, respectively, with the lower H/C ratio (compared to HOA, 2.01) likely attributed to the presence of PAH species (H/C < 1).

Although SFOA contained biomass burning markers, its correlation with acetonitrile (C_2H_3N), a common gas-phase indicator of biomass burning, was weak (r = -0.09), indicating that it should not be classified as a typical BBOA (biomass burning organic aerosol) (Fig. S9b). Instead, SFOA showed stronger correlations with aromatic hydrocarbons such as toluene (r = 0.62) and trimethylbenzene (r = 0.65), suggesting that it is more closely related to petrochemical processes (Fig. S10e-f).

The diurnal variation of SFOA exhibited an inverse relationship with the mixed layer height (MLH), implying strong influence from meteorological conditions, particularly boundary layer dynamics. In contrast to HOA and LO-OOA, which were more influenced by easterly winds, SFOA concentrations were elevated under southerly wind conditions. Notably, several potential sources lie to the south of the sampling site, including petrochemical production facilities, incinerators, and further south, agricultural areas. This spatial pattern, combined with chemical signatures, suggests that SFOA was influenced by both solid fuel combustion emissions, such as those from industrial incinerators, and biomass burning activities in nearby agricultural regions. Additionally, the SFOA factor was strongly correlated with chloride (r = 0.73) (Fig. S9f), consistent with the known chloride emissions from solid fuel combustion, which is widely used in wintertime for power generation, steel manufacturing, and residential heating in the region.

Oxygenated OA (LO-OOA and MO-OOA)

In addition to the two POA factors, two distinct OOA factors were resolved, accounting for an average of 63% of the total OA mass (Fig. S3a). The resolved OOA was further classified into more oxidized oxygenated organic aerosol (MO-OOA, 36%) and less oxidized oxygenated organic aerosol (LO-OOA, 27%), representing different stages of atmospheric aging and oxidation (Jimenez et al., 2009; Ng et al., 2010; Setyan et al., 2012; Xu et al., 2015). According to the triangle plot (Fig. S11), LO-OOA (O/C = 0.53, H/C = 1.65) was located within the region representing fresher SOA with a low f44, while MO-OOA (O/C = 1.03, H/C = 1.28) was associated with more aged and highly oxidized OA, showing a high f44. These characteristics are consistent with previous findings suggesting that freshly formed SOA becomes increasingly oxidized and less volatile with atmospheric aging, transitioning along a continuum from LO-OOA to MO-OOA (Jimenez et al., 2009; Ng et al., 2010).

The secondary nature of both OOA components was further supported by their strong correlations with secondary inorganic aerosol species. As shown in Fig. 2, LO-OOA and MO-OOA exhibited significant correlations with nitrate (r = 0.79 and 0.83, respectively) and sulfate (r = 0.67 and 0.85, respectively). Moreover, the correlation coefficient between total OOA and the sum of secondary inorganic aerosols ($NO_3^- + SO_4^{2-} + NH_4^+$) was as high as 0.96 (Fig. S9e), confirming the association of both LO-OOA and MO-OOA with SOA formation processes.

Temporal variations in the concentrations of LO-OOA and MO-OOA further revealed differences in their source characteristics. LO-OOA showed a distinct morning peak (07:00–08:00, Fig. 2g), indicating influence from local sources. In contrast, MO-OOA exhibited a relatively constant diurnal pattern, (Fig. 2h). Unlike typical wintertime patterns observed in Seoul (Kim et al., 2017), the OOA in the Daesan region displayed a minimum concentration in the afternoon (around 15:00). This suggests that dilution due to the increase in the mixing layer height (MLH) may dominate over photochemical oxidation during this period. Moreover, the similar correlations between Ox (=NO_2+O_3) and MO-OOA/OA during both daytime and nighttime (r=0.52 and r=0.53, respectively) indicate that the Daesan region

is not predominantly influenced by photochemical processes (Fig. 5b). OOA formation in Daesan was further associated with stagnant meteorological conditions, as described in Sect. 3.4. Analysis of BC and MLH revealed that stagnant periods were characterized by a low MLH, during which the SOA fraction within OA increased (Fig. 7). From 15:00 to 22:00, OOA concentrations increased, which could be attributed to the accumulation of aerosols due to the decreasing MLH, as well as the delayed influence of oxidized particles formed during the day. Conversely, the decrease in OOA concentrations between 09:00 and 14:00 coincided with increasing MLH, supporting the interpretation that dilution was the dominant factor during this period.

The LO-OOA was found to be influenced by southeasterly winds and appeared to be more oxidized than primary emissions such as HOA and SFOA. This suggests that it was secondarily formed through atmospheric oxidation of VOCs emitted from processes known to release hydrocarbons, such as petroleum refining and petrochemical production. In addition, the characteristic fragment ions of SFOA (m/z 60 and 73) were also observed in LO-OOA, suggesting that LO-OOA may have been formed, at least in part, through further oxidation of SFOA. This inference is further supported by the polar plot of toluene shown in Fig. S10b. In contrast, the MO-OOA showed higher concentrations under low wind speed conditions and when westerly winds prevailed. This indicates the possibility of particles aging under stagnant conditions.

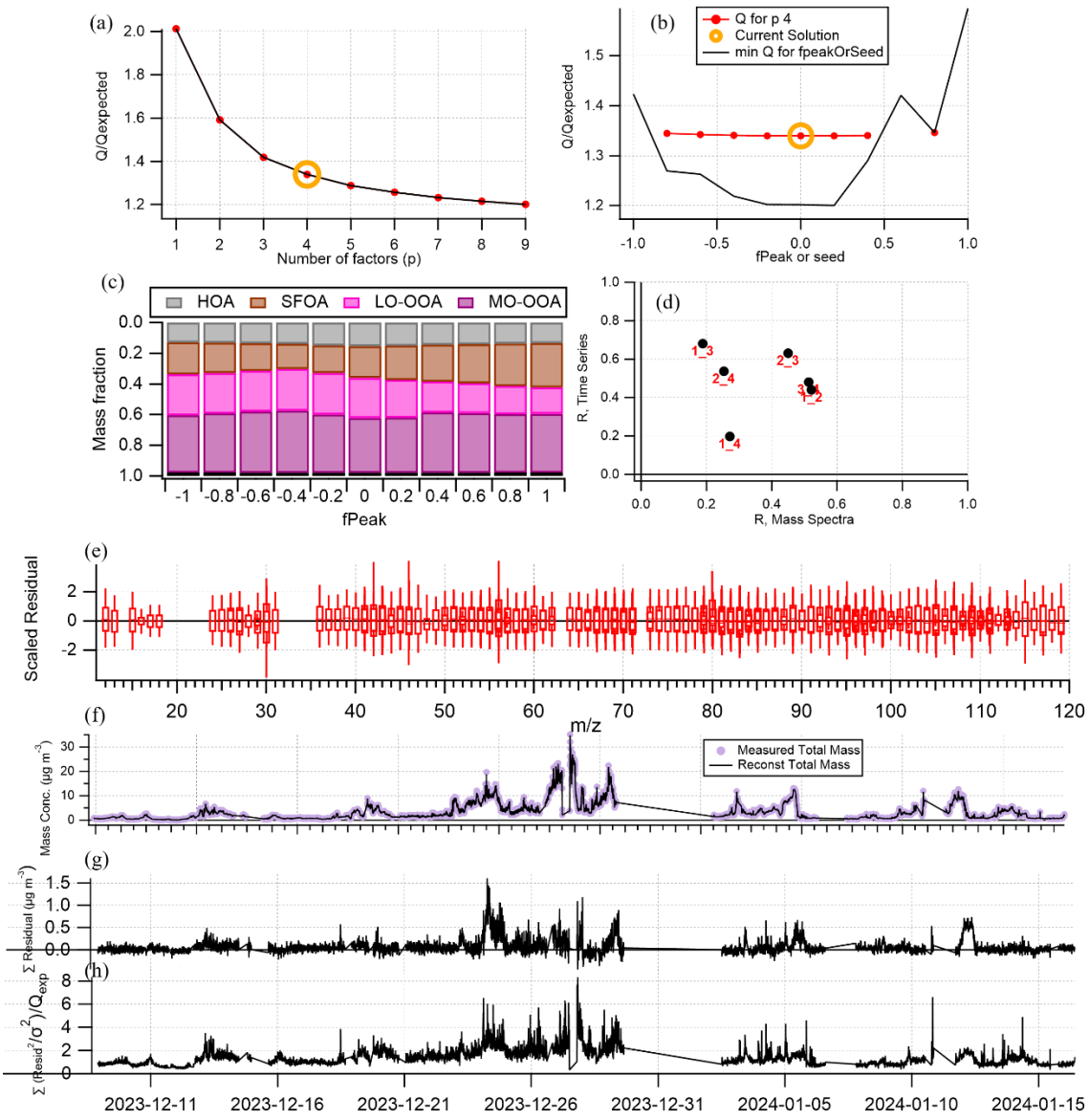

Figure S1 Summary of the key diagnostic plots of the chosen 4-factor solution from PMF analysis of the organic aerosol fraction; (a) Q/Q_{exp} as a function of the number of factors (p) explored in PMF analysis, with the best solution denoted by the open orange circle. Plots b-h are for the chosen solution set, containing 4 factors; (b) Q/Q_{exp} as a function of fPeak; (c) mass fractional contribution to the total OA mass of each of the PMF factors, including the residual (in black), as a function of fPeak; (d) Pearson's r correlation coefficient values for correlations among the time series and mass spectra of the PMF factors. Here, 1=MO-OOA, 2= LO-OOA, 3=SFOA, 4=HOA; (e) box and whiskers plot showing the distributions of scaled residuals for each m/z; (f) time series of the measured organic mass and the recontructed organic mass from the sum of the four OA factors; (g) time series of the variations in the residual (=measured-reconstructed) of the fit; (h) the Q/Q_{exp} for each point in time.

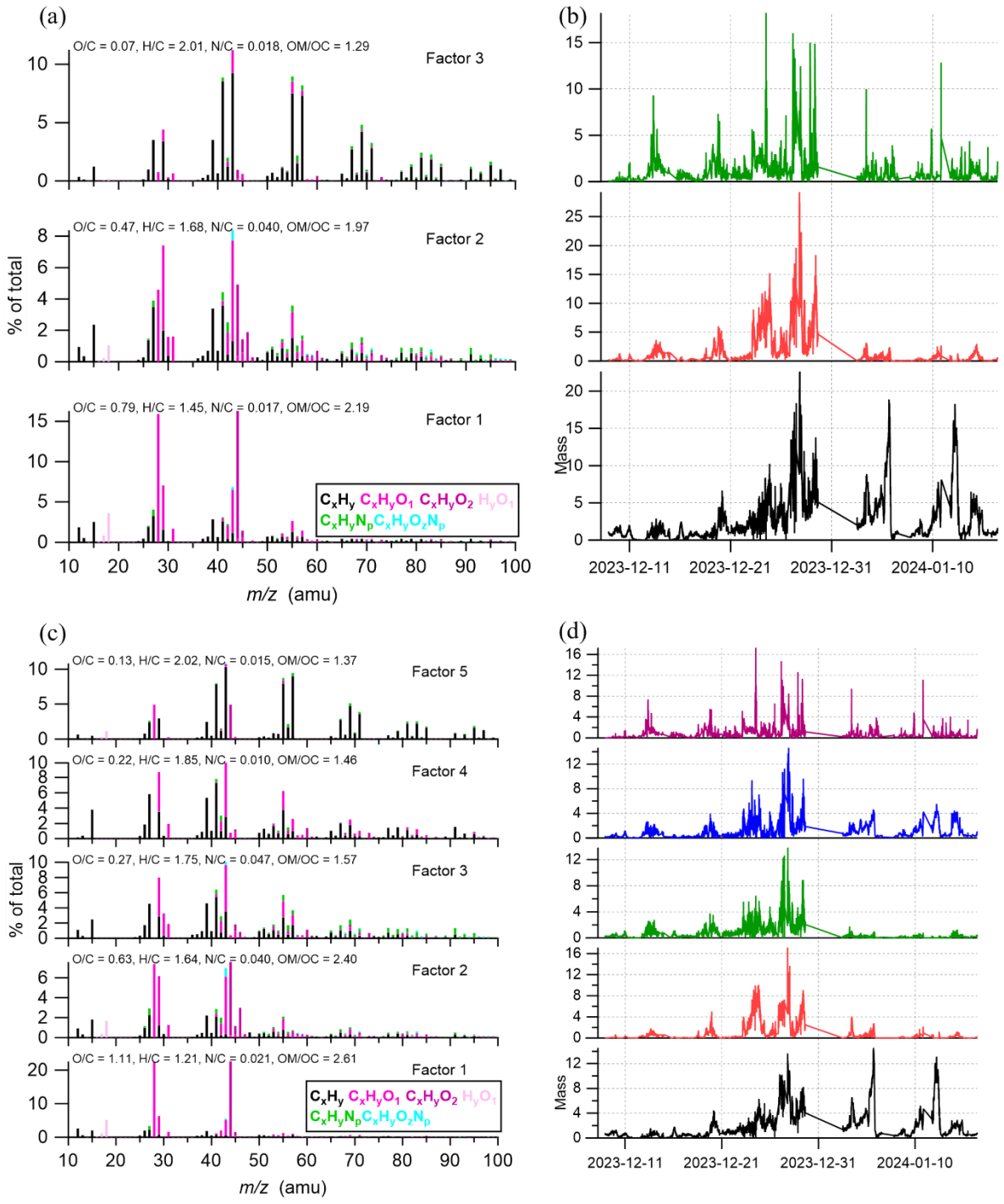

Figure S2 Overview of two other solution sets from PMF analysis: (a,b) High resolution mass spectra and time series of the different OA factors from the 3-factor solution; (c,d) High resolution mass spectra and time series of the different OA factors from the 5-factor solution.

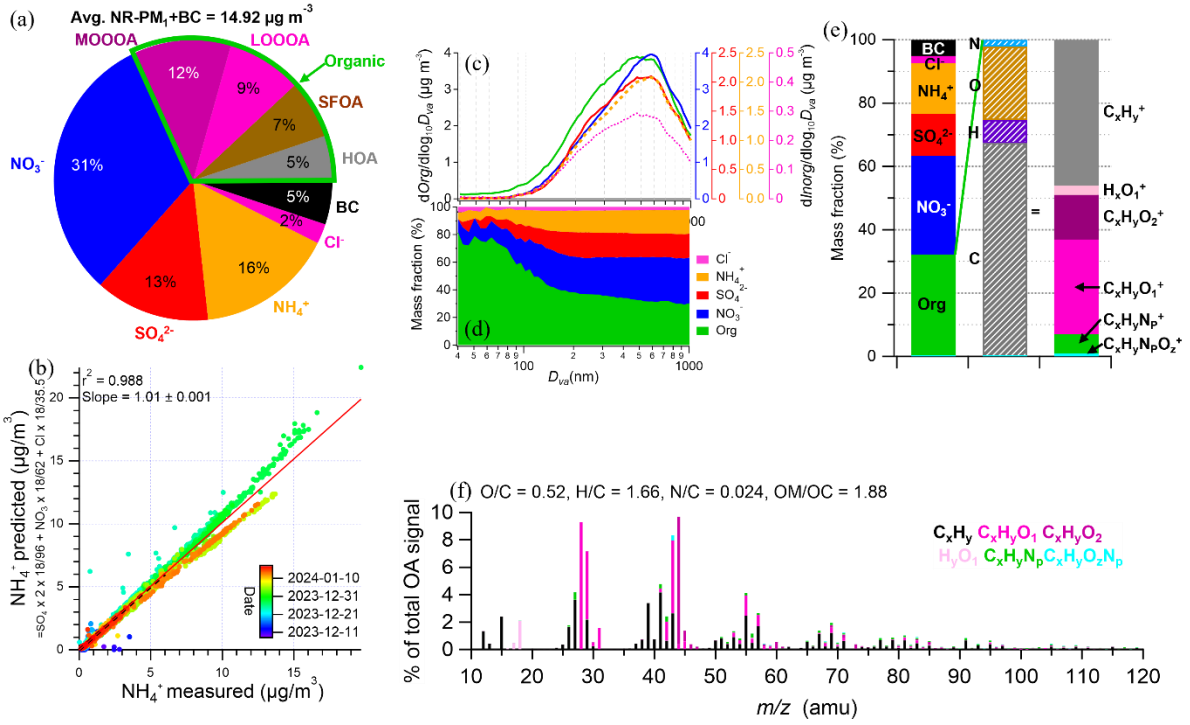

Figure S3 (a) Average compositional pie chart of NR-PM$_1$+BC species (non-refractory PM$_1$ plus black carbon (BC)) and each of the OA factors over the whole campaign. The green outline indicates the fraction of total OA and (b) shows a scatterplot that compares predicted NH_4^+ vs. measured NH_4^+ concentrations. The predicted values were calculated assuming full neutralization of the anions (e.g., sulfate, nitrate, and chloride). The data points are colored by organic concentrations. (c) Campaign-averaged size distributions for individual NR-PM$_1$ species; (d) averaged mass fractional contributions of each NR-PM$_1$ species to the total NR-PM$_1$ mass as a function of size. (e) Overview of the average PM$_1$ and OA compositions in Daesan during winter; (f) average high-resolution mass spectrum of OA colored by the different ion families. The average elemental ratios for the OA fraction are described.

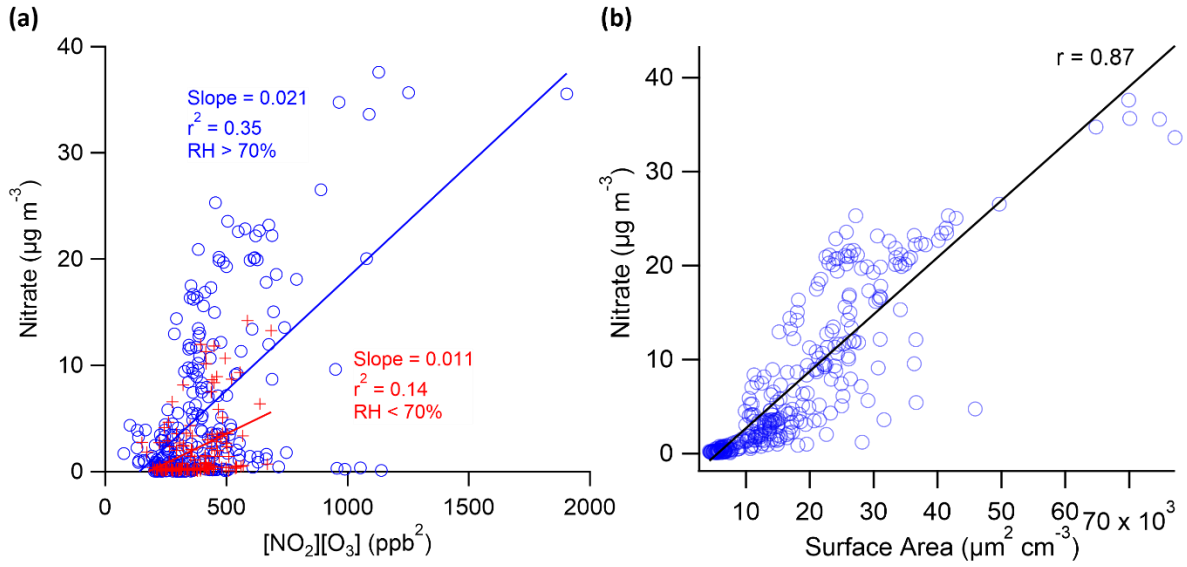

Figure S4 (a) Scatterplot between nitrate and $[NO_2][O_3]$ under different RH conditions. Data are shown for RH > 70% (blue) and < 70% (red) (b) Scatterplot of nitrate concentration versus particle surface area measured by SMPS, with a linear regression fit (solid line).

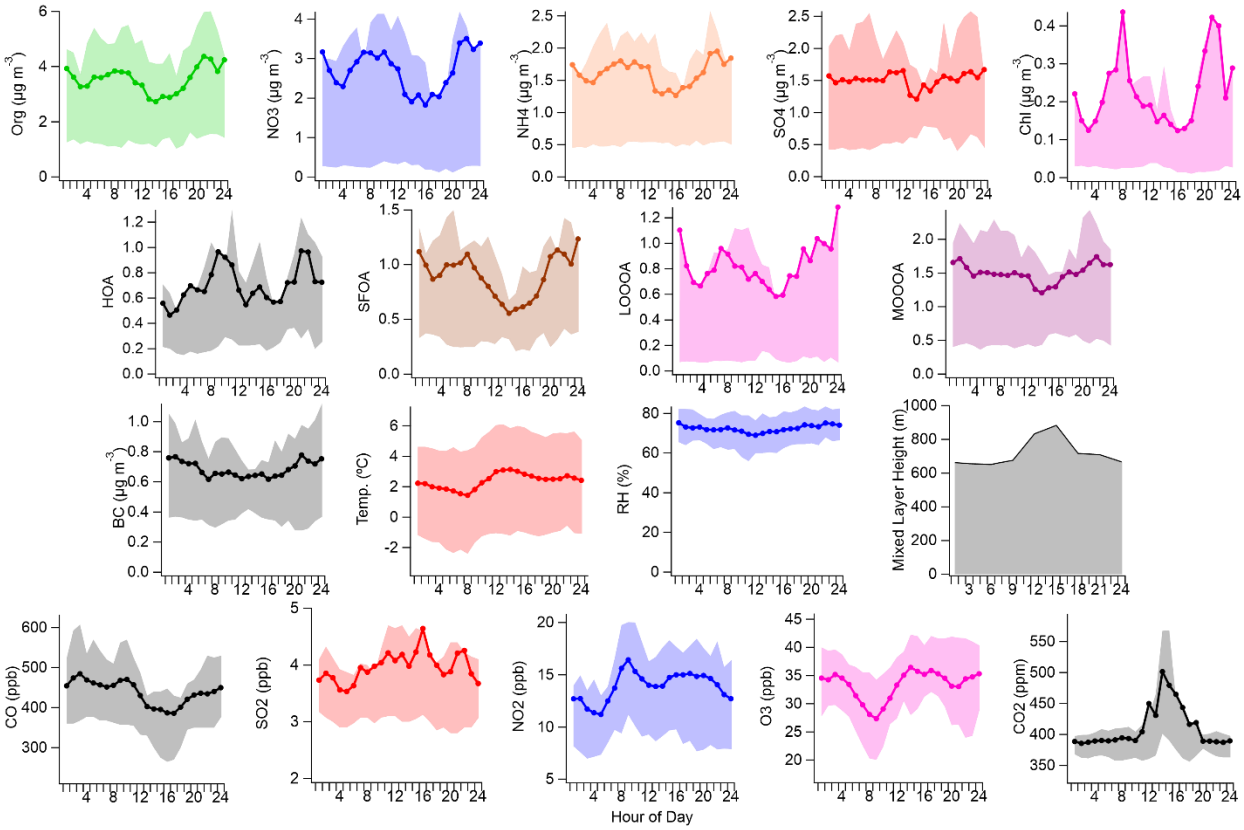

Figure S5 Average diurnal profiles for the PM_1 species measured by the aerosol mass spectrometer (AMS) and Aethalometer, various meteorological parameters, and various gas phase species. The solid line with markers represents the mean values, while the shaded regions denote the interquartile range (25th-75th percentiles).

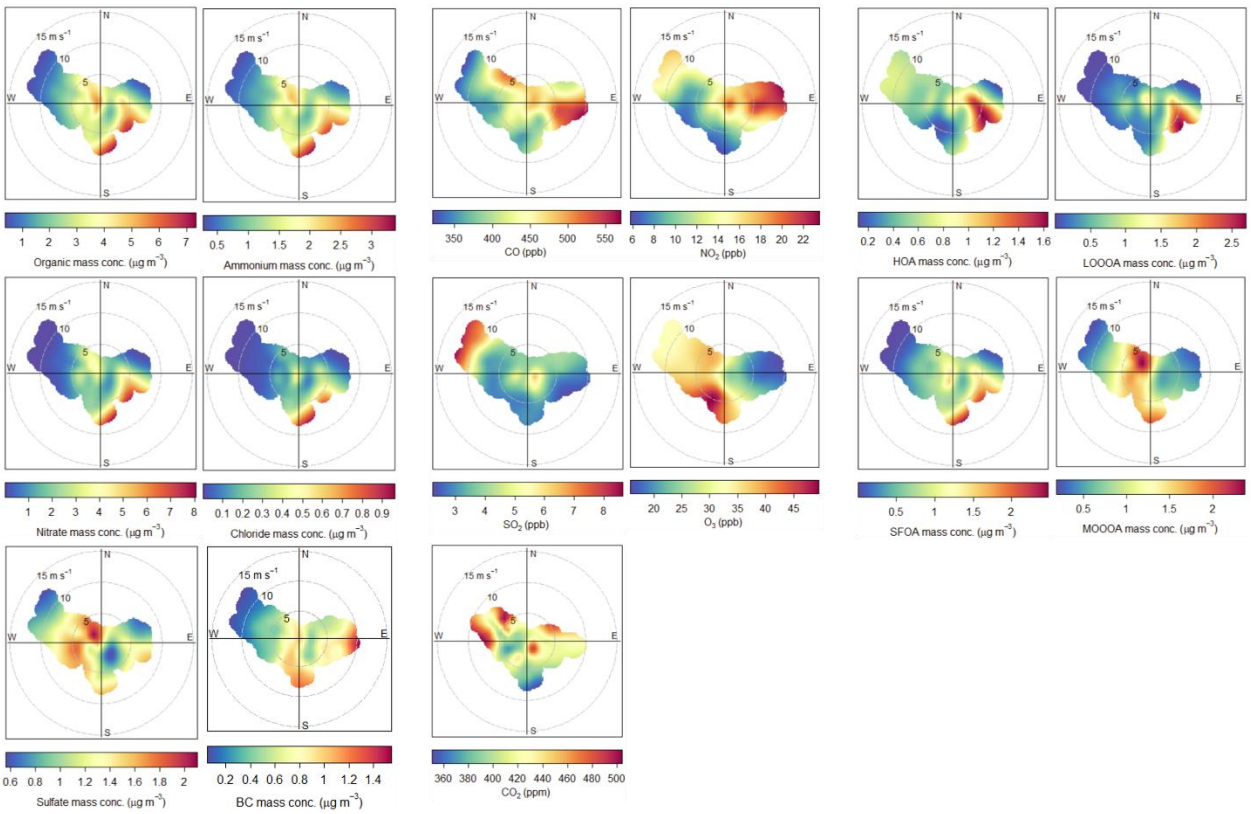

Figure S6 Polar plots of hourly averaged PM_1+BC species concentrations, the mixing ratios of various gas-phase species, and mass concentrations of the four OA factors identified from PMF analysis as a function of WS and direction

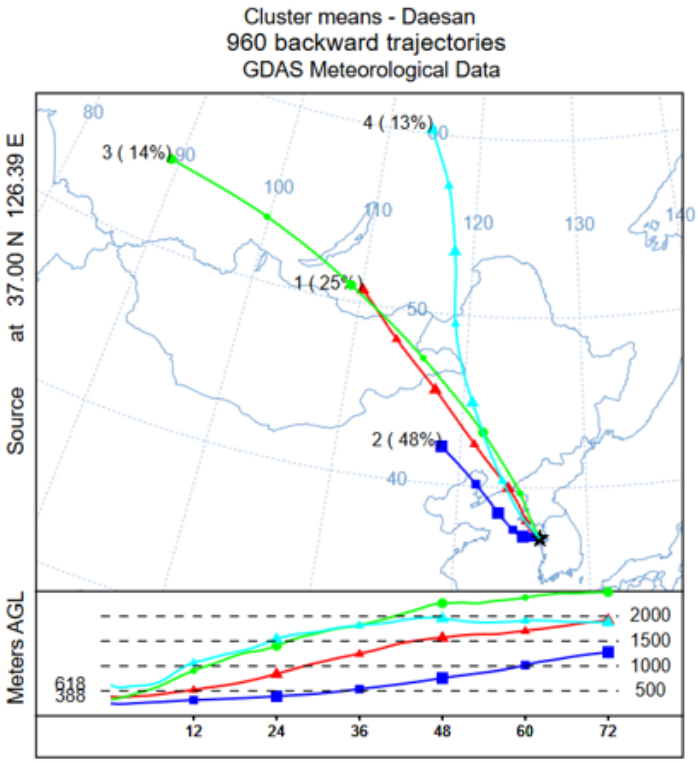

Figure S7 The trajectories were released at half of the mixing height at the Daesan (latitude: 37.00°N, longitude: 126.39°E). The average arrival heights of the back trajectories for were approximately 388 m and 618 m

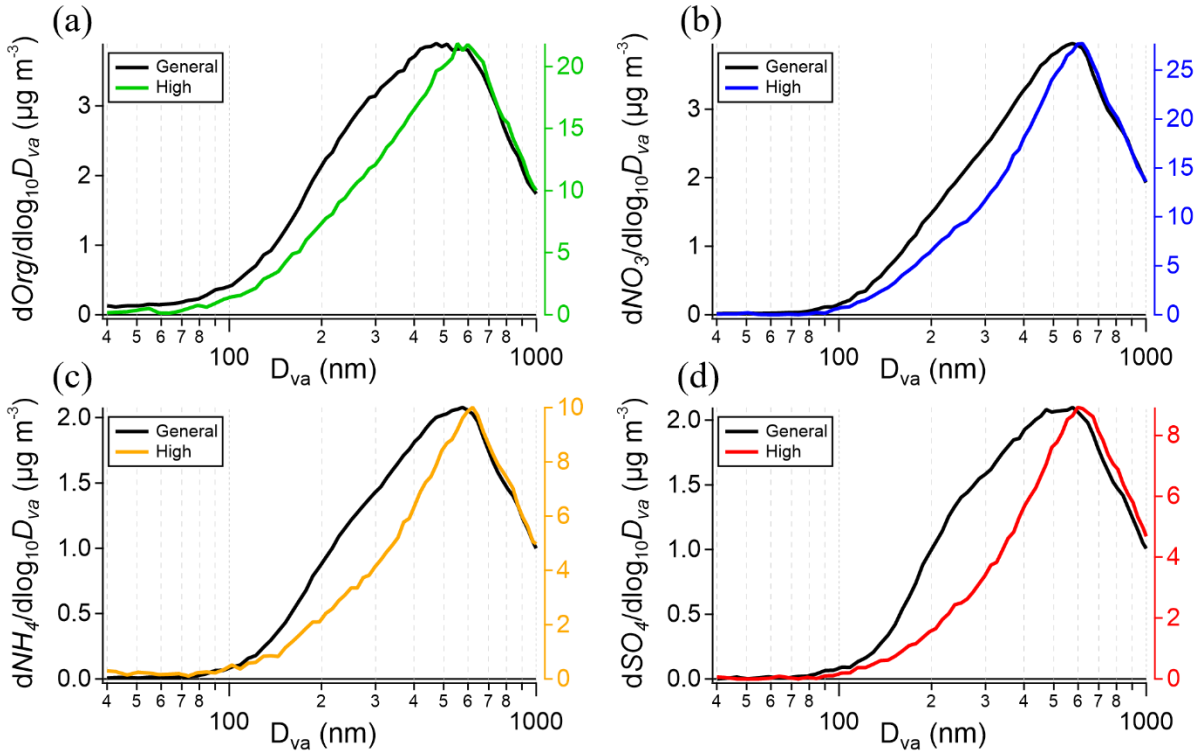

Figure S8 Averaged mass-based size distribution of (a) organic, (b) nitrate, (c) ammonium, and (d) sulfate during general days (black line) and high concentration days (color line)

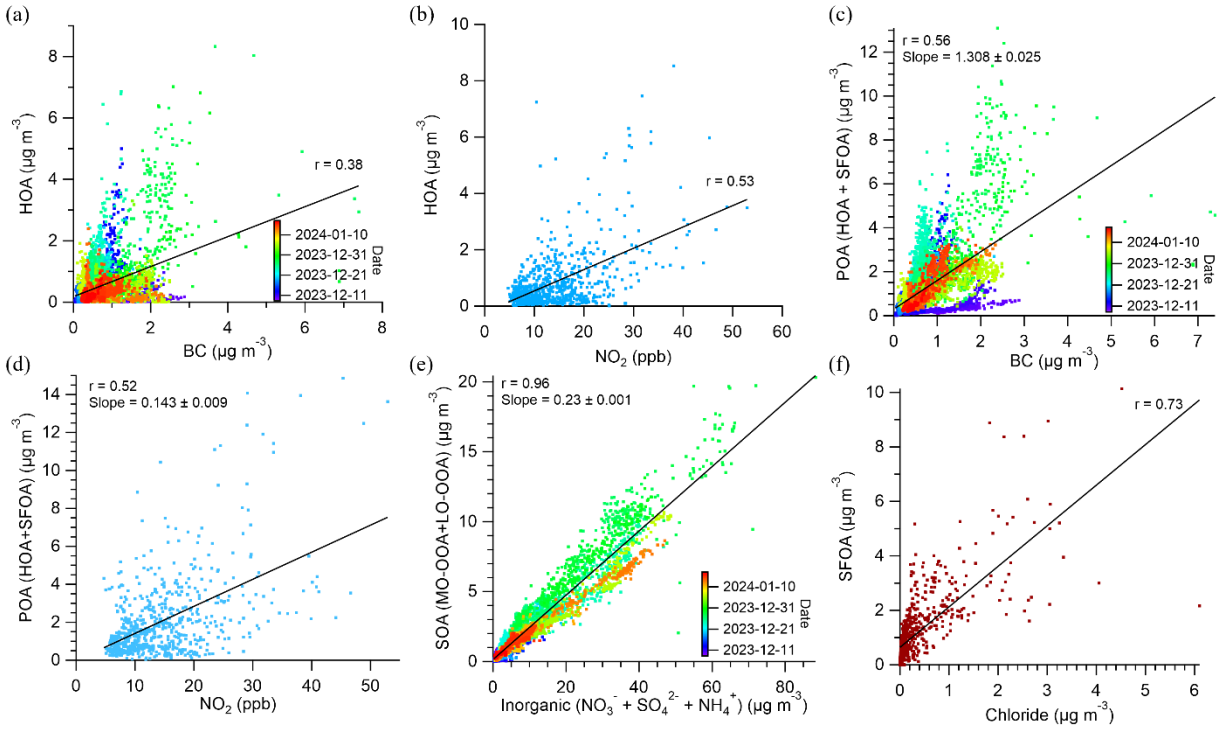

Figure S9 Scatterplot between (a) HOA and BC, (b) HOA and NO_2, (c) POA and BC, (d) POA and NO_2, and (e) SOA and inorganic

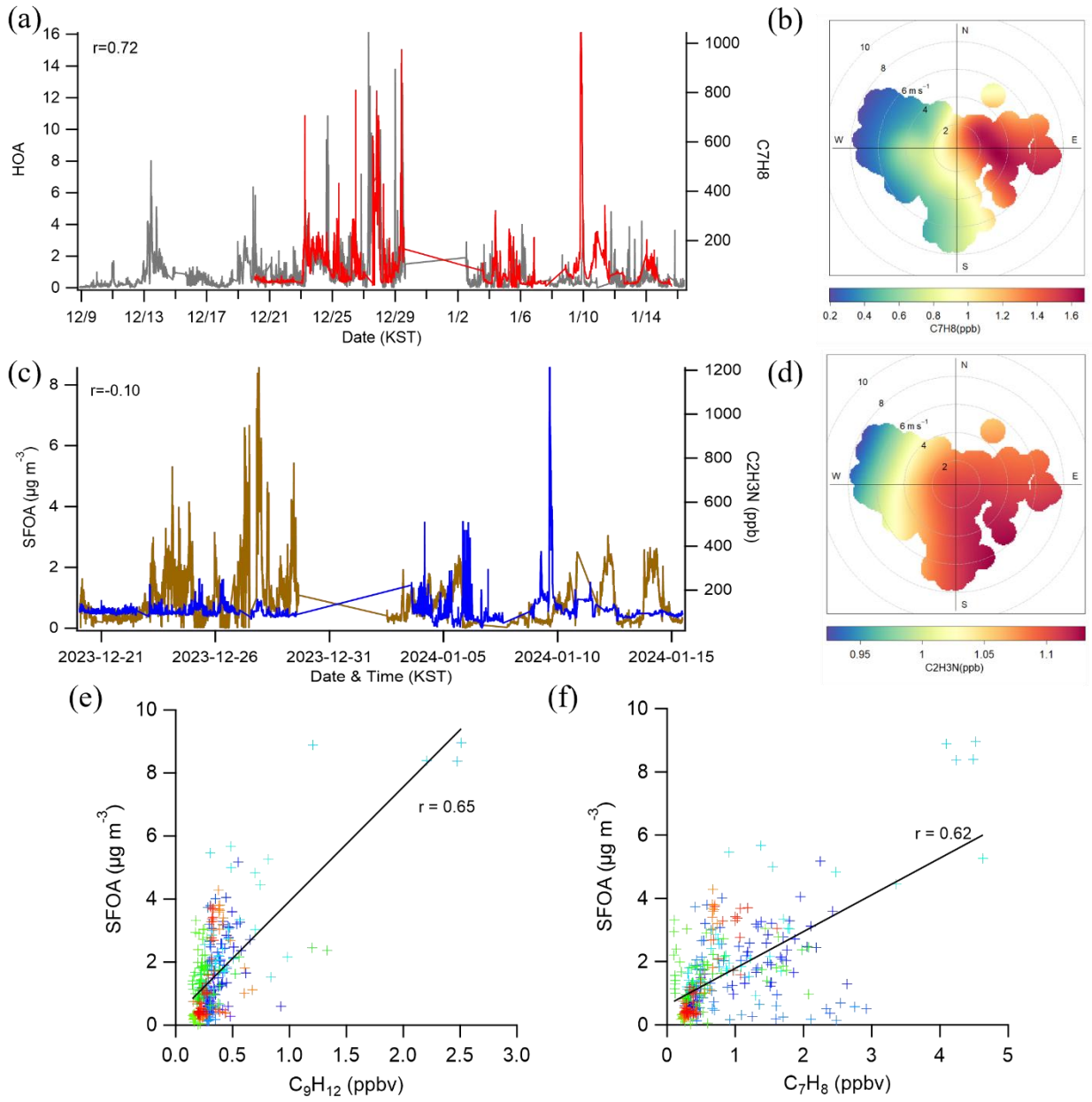

Figure S10 (a) Correlation between toluene and HOA; (b) Polar plot of toluene; (c) Correlation between acetonitrile and SFOA; (d) Polar plot of acetonitrile; (e) Correlation between Trimethylbenzene and SFOA; (f) Correlation between toluene and SFOA

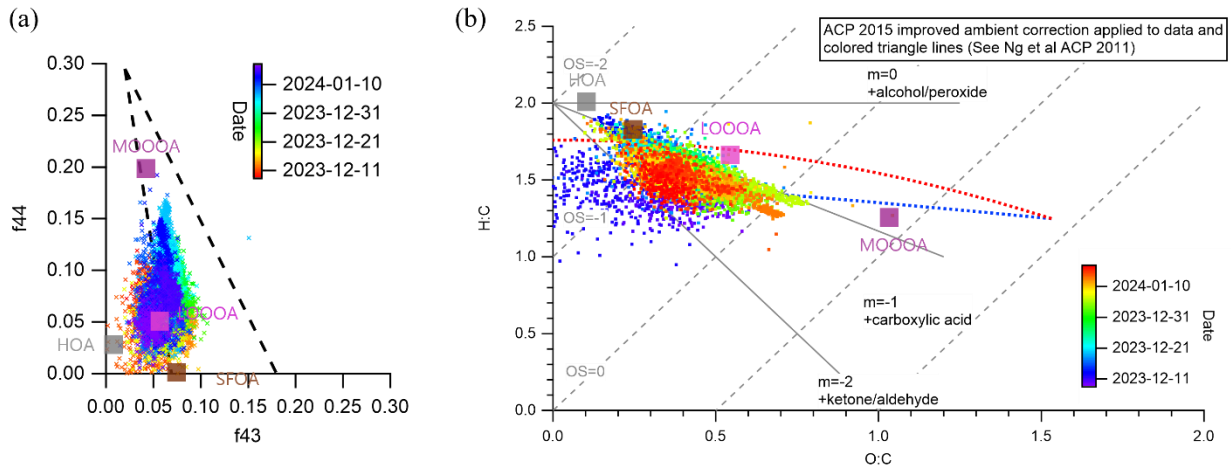

Figure S11 (a) Triangular plot of f_{44} versus f_{43} and (b) Van Krevelen diagram for four OA factors and all of the measured OA data (dots), colored by the time of the day

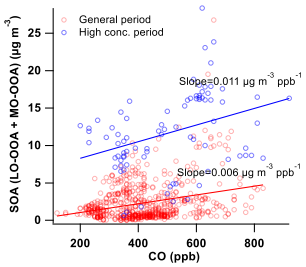

Figure S12 Scatter plot of SOA concentration as a function of CO concentration for different periods, with linear regression fits (solid lines) for each dataset.

Table S1 Average (±1 standard deviation), minimum, and maximum concentrations of the PM_1+BC species and the total PM_1+BC mass over the whole campaign, and the average contribution of each of the PM_1+BC species to the total PM_1+BC mass

	Average conc.±1 SD.	Min	Max	Fraction	Detection limit(3m/6m)
Organic	4.72±4.91	0.01	50.47	32	0.07/0.05
Nitrate	4.51±6.74	0.00	54.18	31	0.02/0.02
Sulfate	1.96±1.88	0.00	15.84	13	0.01/0.01
Ammonium	2.31±2.69	0.12	19.85	16	0.05/0.04
Chloride	0.33±0.70	0.00	11.04	2	0.005/0.003
Black carbon	0.75±0.57	0.00	7.67	5	
Total	14.58±16.44	0.73	142.73	-	

Reference

Alfarra, M. R., Prevot, A. S. H., Szidat, S., Sandradewi, J., Weimer, S., Lanz, V. A., Schreiber, D., Mohr, M., & Baltensperger, U. (2007). Identification of the Mass Spectral Signature of Organic Aerosols from Wood Burning Emissions. *Environmental Science & Technology*, *41*(16), 5770-5777. https://doi.org/10.1021/es062289b

Allan, J. D., Williams, P. I., Morgan, W. T., Martin, C. L., Flynn, M. J., Lee, J., Nemitz, E., Phillips, G. J., Gallagher, M. W., & Coe, H. (2010). Contributions from transport, solid fuel burning and cooking to primary organic aerosols in two UK cities. *Atmos. Chem. Phys.*, *10*(2), 647-668. https://doi.org/10.5194/acp-10-647-2010

Canagaratna, M. R., Jimenez, J. L., Kroll, J. H., Chen, Q., Kessler, S. H., Massoli, P., Hildebrandt Ruiz, L., Fortner, E., Williams, L. R., Wilson, K. R., Surratt, J. D., Donahue, N. M., Jayne, J. T., & Worsnop, D. R. (2015). Elemental ratio measurements of organic compounds using aerosol mass spectrometry: characterization, improved calibration, and implications. *Atmos. Chem. Phys.*, *15*(1), 253-272. https://doi.org/10.5194/acp-15-253-2015

Huang, X. F., He, L. Y., Hu, M., Canagaratna, M. R., Sun, Y., Zhang, Q., Zhu, T., Xue, L., Zeng, L. W., Liu, X. G., Zhang, Y. H., Jayne, J. T., Ng, N. L., & Worsnop, D. R. (2010). Highly time-resolved chemical characterization of atmospheric submicron particles during 2008 Beijing Olympic Games using an Aerodyne High-Resolution Aerosol Mass Spectrometer. *Atmos. Chem. Phys.*, *10*(18), 8933-8945. https://doi.org/10.5194/acp-10-8933-2010

Jeon, J., Chen, Y., & Kim, H. (2023). Influences of meteorology on emission sources and physicochemical properties of particulate matter in Seoul, Korea during the heating period. *Atmospheric Environment*, *303*, 119733. https://doi.org/https://doi.org/10.1016/j.atmosenv.2023.119733

Jimenez, J. L., Canagaratna, M. R., Donahue, N. M., Prevot, A. S. H., Zhang, Q., Kroll, J. H., DeCarlo, P. F., Allan, J. D., Coe, H., Ng, N. L., Aiken, A. C., Docherty, K. S., Ulbrich, I. M., Grieshop, A. P., Robinson, A. L., Duplissy, J., Smith, J. D., Wilson, K. R., Lanz, V. A.,…Worsnop, D. R. (2009). Evolution of Organic Aerosols in the Atmosphere. *Science*, *326*(5959), 1525-1529. https://doi.org/doi:10.1126/science.1180353

Kim, H., Zhang, Q., Bae, G. N., Kim, J. Y., & Lee, S. B. (2017). Sources and atmospheric processing of winter aerosols in Seoul, Korea: insights from real-time measurements using a high-resolution aerosol mass spectrometer. *Atmos. Chem. Phys.*, *17*(3), 2009-2033. https://doi.org/10.5194/acp-17-2009-2017

Lanz, V. A., Alfarra, M. R., Baltensperger, U., Buchmann, B., Hueglin, C., Szidat, S., Wehrli, M. N., Wacker, L., Weimer, S., Caseiro, A., Puxbaum, H., & Prevot, A. S. H. (2008). Source Attribution of Submicron Organic Aerosols during Wintertime Inversions by Advanced Factor Analysis of Aerosol Mass Spectra. *Environmental Science & Technology*, *42*(1), 214-220. https://doi.org/10.1021/es0707207

Morgan, W. T., Allan, J. D., Bower, K. N., Highwood, E. J., Liu, D., McMeeking, G. R., Northway, M. J., Williams, P. I., Krejci, R., & Coe, H. (2010). Airborne measurements of the spatial distribution of aerosol chemical composition across Europe and evolution of the organic fraction. *Atmos. Chem. Phys.*, *10*(8), 4065-4083. https://doi.org/10.5194/acp-10-4065-2010

Ng, N. L., Canagaratna, M. R., Jimenez, J. L., Zhang, Q., Ulbrich, I. M., & Worsnop, D. R. (2011). Real-Time Methods for Estimating Organic Component Mass Concentrations from Aerosol Mass Spectrometer Data. *Environmental Science & Technology*, *45*(3), 910-916. https://doi.org/10.1021/es102951k

Ng, N. L., Canagaratna, M. R., Zhang, Q., Jimenez, J. L., Tian, J., Ulbrich, I. M., Kroll, J. H., Docherty, K. S., Chhabra, P. S., Bahreini, R., Murphy, S. M., Seinfeld, J. H., Hildebrandt, L., Donahue, N. M., DeCarlo, P. F., Lanz, V. A., Prévôt, A. S. H., Dinar, E., Rudich, Y., & Worsnop, D. R. (2010). Organic aerosol components observed in Northern Hemispheric datasets from Aerosol Mass Spectrometry. *Atmos. Chem. Phys.*, *10*(10), 4625-4641. https://doi.org/10.5194/acp-10-4625-2010

Setyan, A., Zhang, Q., Merkel, M., Knighton, W. B., Sun, Y., Song, C., Shilling, J. E., Onasch, T. B., Herndon, S. C., Worsnop, D. R., Fast, J. D., Zaveri, R. A., Berg, L. K., Wiedensohler, A., Flowers, B. A., Dubey, M. K., & Subramanian, R. (2012). Characterization of submicron particles influenced by mixed biogenic and anthropogenic emissions using high-resolution aerosol mass spectrometry: results from CARES. *Atmos. Chem. Phys.*, *12*(17), 8131-8156. https://doi.org/10.5194/acp-12-8131-2012

Sun, Y. L., Zhang, Q., Schwab, J. J., Demerjian, K. L., Chen, W. N., Bae, M. S., Hung, H. M., Hogrefe, O., Frank, B., Rattigan, O. V., & Lin, Y. C. (2011). Characterization of the sources and processes of organic and inorganic aerosols in New York city with a high-resolution time-of-flight aerosol mass apectrometer. *Atmos. Chem. Phys.*, *11*(4), 1581-1602. https://doi.org/10.5194/acp-11-1581-2011

Tobler, A. K., Skiba, A., Canonaco, F., Močnik, G., Rai, P., Chen, G., Bartyzel, J., Zimnoch, M., Styszko, K., Nęcki, J., Furger, M., Różański, K., Baltensperger, U., Slowik, J. G., & Prevot, A. S. H. (2021). Characterization of

non-refractory (NR) PM1 and source apportionment of organic aerosol in Kraków, Poland. *Atmos. Chem. Phys.*, *21*(19), 14893-14906. https://doi.org/10.5194/acp-21-14893-2021

Xu, L., Guo, H., Boyd, C. M., Klein, M., Bougiatioti, A., Cerully, K. M., Hite, J. R., Isaacman-VanWertz, G., Kreisberg, N. M., Knote, C., Olson, K., Koss, A., Goldstein, A. H., Hering, S. V., de Gouw, J., Baumann, K., Lee, S.-H., Nenes, A., Weber, R. J., & Ng, N. L. (2015). Effects of anthropogenic emissions on aerosol formation from isoprene and monoterpenes in the southeastern United States. *Proceedings of the National Academy of Sciences*, *112*(1), 37-42. https://doi.org/doi:10.1073/pnas.1417609112

Zhang, Q., Alfarra, M. R., Worsnop, D. R., Allan, J. D., Coe, H., Canagaratna, M. R., & Jimenez, J. L. (2005). Deconvolution and Quantification of Hydrocarbon-like and Oxygenated Organic Aerosols Based on Aerosol Mass Spectrometry. *Environmental Science & Technology*, *39*(13), 4938-4952. https://doi.org/10.1021/es0485681